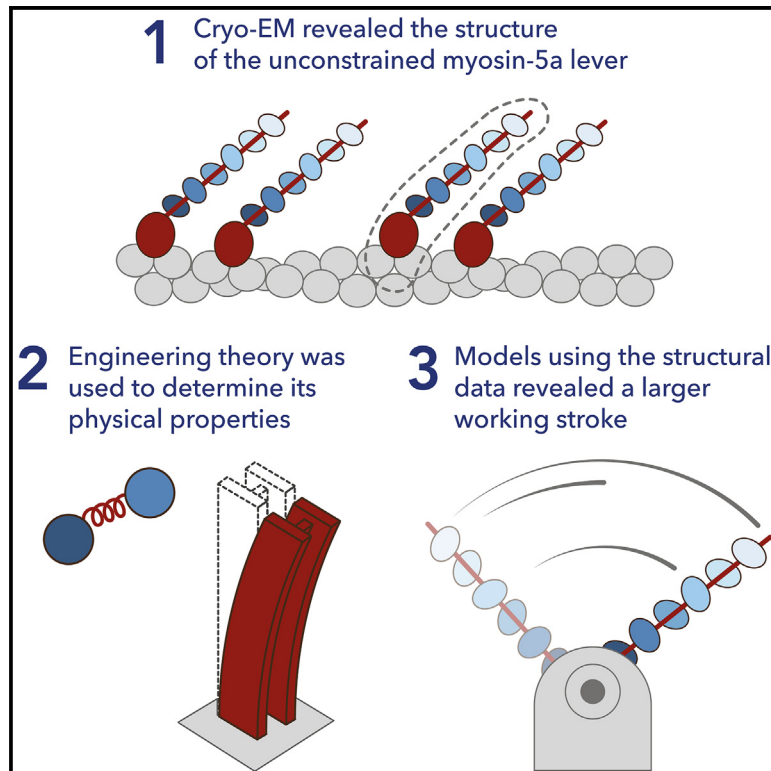


Structure

Exploiting cryo-EM structures of actomyosin-5a to reveal the physical properties of its lever

Graphical abstract



Authors

Molly S.C. Gravett, David P. Klebl, Oliver G. Harlen, Daniel J. Read, Stephen P. Muench, Sarah A. Harris, Michelle Peckham

Correspondence

m.s.c.gravett@uu.nl (M.S.C.G.),
m.peckham@leeds.ac.uk (M.P.)

In brief

Gravett et al. determined the structure of the motor Myo5a with a full-length lever bound to actin. The lever conformations captured in their data revealed lever flexibility varies along its length. Modeling the working stroke of Myo5a suggests it closely matches the helicity of the actin track.

Highlights

- Cryo-EM structure of single-headed Myo5a with its full lever, bound to actin
- Multiple lever conformations show intrinsic flexibility of the Myo5a lever
- Flexibility varies along the length of the lever
- Modeling using multiple lever conformations reveals a 35 nm working stroke



Article

Exploiting cryo-EM structures of actomyosin-5a to reveal the physical properties of its lever

Molly S.C. Gravett,^{1,2,3,6,*} David P. Klebl,^{1,4,7} Oliver G. Harlen,⁵ Daniel J. Read,⁵ Stephen P. Muench,^{1,4} Sarah A. Harris,^{1,3,8} and Michelle Peckham^{1,2,9,*}

¹Astbury Centre for Structural Molecular Biology, University of Leeds, LS2 9JT Leeds, UK

²School of Molecular and Cellular Biology, University of Leeds, LS2 9JT Leeds, UK

³School of Physics and Astronomy, University of Leeds, LS2 9JT Leeds, UK

⁴School of Biomedical Sciences, University of Leeds, LS2 9JT Leeds, UK

⁵School of Mathematics, University of Leeds, LS2 9JT Leeds, UK

⁶Present address: Structural Biochemistry, Department of Chemistry, Bijvoet Centre for Biomolecular Research, Utrecht University, Utrecht, Netherlands

⁷Present address: Department of Cell and Virus Structure, Max Planck Institute of Biochemistry, Martinsried, Germany

⁸Present address: School of Mathematical and Physical Sciences, E15, Hicks Building, Hounsfield Road, University of Sheffield, S3 7RH Sheffield, UK

⁹Lead contact

*Correspondence: m.s.c.gravett@uu.nl (M.S.C.G.), m.peckham@leeds.ac.uk (M.P.)

<https://doi.org/10.1016/j.str.2024.09.025>

SUMMARY

Myosin 5a (Myo5a) is a dimeric processive motor protein that transports cellular cargos along filamentous actin (F-actin). Its long lever is responsible for its large power-stroke, step size, and load-bearing ability. Little is known about the levers' structure and physical properties, and how they contribute to walking mechanics. Using cryoelectron microscopy (cryo-EM) and molecular dynamics (MD) simulations, we resolved the structure of monomeric Myo5a, comprising the motor domain and full-length lever, bound to F-actin. The range of its lever conformations revealed its physical properties, how stiffness varies along its length and predicts a large, 35 nm, working stroke. Thus, the newly released trail head in a dimeric Myo5a would only need to perform a small diffusive search for its new binding site on F-actin, and stress would only be generated across the dimer once phosphate is released from the lead head, revealing new insight into the walking behavior of Myo5a.

INTRODUCTION

Myosins comprise a large family of cytoskeletal motors with a diverse range of biological functions.^{1–3} Each myosin comprises an N-terminal motor domain, which contains a nucleotide and an F-actin (filamentous-actin) binding site, followed by a lever, which comprises the converter and a light chain binding region. The C-terminal tail is composed of specific domains that dictate the cellular function of the myosin. Small-scale conformational changes in the motor, driven by nucleotide state and F-actin binding, are amplified into a large-scale lever movement, which drives the movement of myosin along F-actin. Thus, myosin efficiently uses ATP hydrolysis to drive directional force and motion along its track.

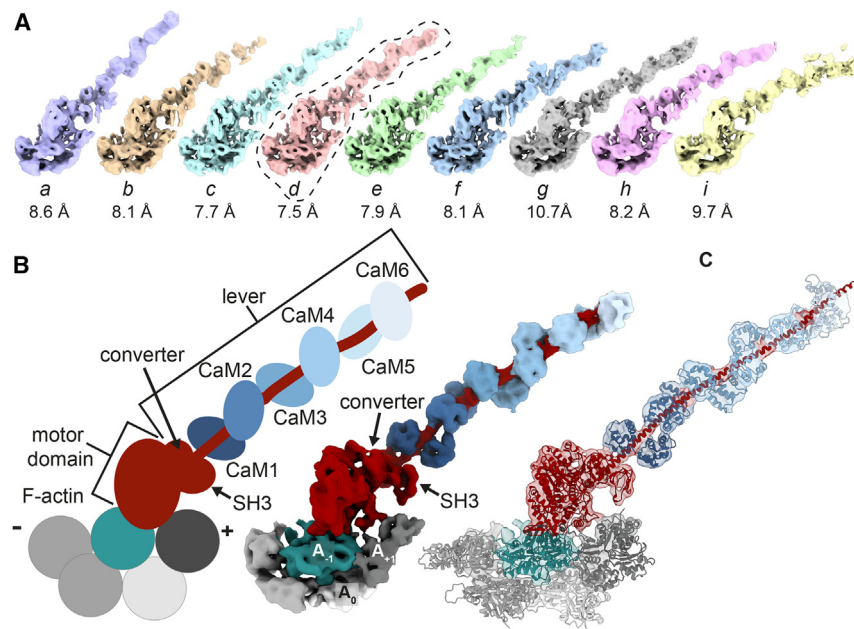
The mechanics of motors operating at the nanoscale are largely different from macroscopic motors, due to the viscosity of their environment, and the fact they are subject to thermal fluctuations and Brownian motion.^{4,5} There is only a limited understanding of how small-scale changes at the active site of the motor are translated into large-scale coordinated movements of the lever. It is unclear what the range of lever conformations available to the motor is, how lever compliance varies along the lever,

and how these properties contribute to the lever movement and thus the working stroke. Here we address these questions using Myosin-5a (Myo5a), a widely expressed myosin,⁶ and provide evidence for the flexibility and conformational variability of the lever and hypothesize how this may contribute to its working stroke and walking behavior.

Myo5a is a dimeric motor that walks processively along F-actin toward its barbed end,⁷ taking multiple steps without dissociating.^{8,9} Its two heads are dimerized by a coiled-coil tail, and it is recruited to cargo via its C-terminal cargo binding domain.⁶ Its long lever is composed of the converter followed by an α -helix that includes 6 IQ (isoleucine-glutamine) motifs, each occupied by a calmodulin light chain (CaM). This enables this myosin to take large, 36 nm, steps along F-actin, that approximate the \sim 36 nm helical repeat of the actin filament,¹⁰ thus minimizing azimuthal distortion.^{8,9} Its ability to take multiple steps without dissociating arises from its ATPase mechanism, in which ADP, not phosphate (Pi) release, is the rate limiting step.¹¹ As a result, Myo5a has a high duty ratio, which means that each head spends most of its ATPase cycle bound to F-actin.¹²

The step size of Myo5a is 36 nm, however, its working stroke is estimated to be only 25 nm, composed of 20 nm from P_i release,





dark gray for the F-actin subunit closest to the plus end (A_{+1}). The cryo-EM split map (contour level: 0.25) is shown for a single Myo5a S1 class (class *d*) with the full-length lever (global resolution of 7.5 Å at 0.143 FSC).

(C) The pseudoatomic model of Myo5a S1 is shown fitted into the split map (from B).

followed by ~ 5 nm from ADP release.¹² When both heads are bound to F-actin, the lead head remains in its pre-powerstroke conformation after P_i release and can only complete its powerstroke when the trail head detaches.¹³ This is thought to lead to an internal strain between the two attached heads of ~ 2 pN.¹⁴ The internal strain is thought to slow ADP release from the lead head by ~ 250 times compared to the trail head, a process known as gating.¹⁵ This prevents premature release of ADP from the lead head, and biases ATP binding to the trail head followed by its detachment and a rapid diffusive search for its next F-actin binding site (estimated as ~ 11 nm in $100 \mu\text{s}$ ¹²), enabling continuous forward motion.

The mechanical properties of the Myo5a lever are thus critical for its walking behavior. It must be able to accommodate internal strain (or deformation) to co-ordinate and promote forward stepping, and able to resist a stall force of ~ 3 pN that prevents forward motion.⁸ To gain a better understanding of the mechanical properties of the lever, we have used cryoelectron microscopy (cryo-EM) to generate high resolution 3D structures of a single-headed Myo5a construct, composed of the motor domain and a full-length 6IQ lever (S1), bound to F-actin. By resolving multiple conformations of Myo5a S1 from a single cryo-EM dataset we have uncovered the intrinsic flexibility of the molecule, determined the lever stiffness in 3D, and identified regions of compliancy along its length. This allows us to interpret how lever flexibility may influence the working stroke of Myo5a.

RESULTS AND DISCUSSION

3D cryo-EM classification captures 9 classes with levers in variable positions

To investigate the flexibility of the lever of Myo5a S1, we used cryo-EM to determine its structure when bound to F-actin in

Figure 1. Cryo-EM shows the lever variability in Myo5a S1

(A) Cryo-EM maps for the nine 3D classes that were generated (contour level: 0.28). All classes showed density for all 6 CaMs. Breaks in density for CaM5 and 6 in some classes (e.g., *b*) do not appear if the molecules are displayed using lower thresholds. Classes are displayed in order of lever bend along the F-actin longitudinal axis. The estimate of the masked global resolution at 0.143 FSC (Fourier Shell Correlation) is displayed beneath each class. The circled class (*d*) is the class with the best resolution that was selected for generating the pseudoatomic model.

(B) Shows a diagram with the color scheme used here in all figures, together with the cryo-EM split map. The myosin heavy chain is shown in red, and each of the 6 calmodulin light chains (CaMs) are shown in shades of blue, and labeled CaM 1–6, where the number refers to which IQ motif the CaM is bound. The polarity of F-actin is indicated by + for the plus and – for the minus end of the filament. The two adjacent F-actin subunits that interact with the motor domain are colored green for the F-actin subunit closest to the minus end (A_{-1}), and

rigor. Previous cryo-EM studies of Myo5a-1IQ bound to F-actin¹⁶ have shown a continuous conformational heterogeneity that was lower in rigor than in the ADP state. Thus, we chose the rigor state to optimize the chances of resolving multiple conformations of the lever. Focusing on a single Myo5a S1 and a single F-actin subunit allowed us to generate a 3D reconstruction that resolved the entire lever.

3D classification of Myo5a S1 molecules bound to F-actin resulted in 9 classes, in which density for the whole lever could be observed (Figure 1A). The position of the motor is unchanged between the classes while the position and conformation of lever changes from *a* to *i* (Figure 1A). These classes likely represent snapshots of the lever across the range of continuous motion that the lever can undergo, reflecting the flexibility of the lever. The number of particles in each class is similar, and the global resolution of each class varied from 7.5 Å (class *d*) to 10.7 Å (Figures 1A and S1). Classes in which the lever angles are shallow are not due to compression in the ice as side views contribute to the reconstruction of each class (Figure S2). Side views are only possible if the lever is lying in plane with the ice layer.

Within each of the 9 classes, the resolution of the cryo-EM density map along the lever decreased moving away from the motor. For example, in class *d* the global resolution decreased from ~ 7 to 25 Å, from the converter to IQ6 (Figure S1B). This reflects conformational heterogeneity even within a single class, again demonstrating the flexibility within the lever. Using the cryo-EM data to perform an initial refinement that focused on a single motor domain and the first IQ generated a 4.2 Å reconstruction that was similar in structure to that previously reported for chicken Myo5a¹⁶ with a single IQ motif bound to F-actin in rigor (Figure S3). Small differences in the F-actin structure in our reconstruction compared to that in the earlier report¹⁶ likely arise from our use of F-actin that was not phalloidin stabilized.

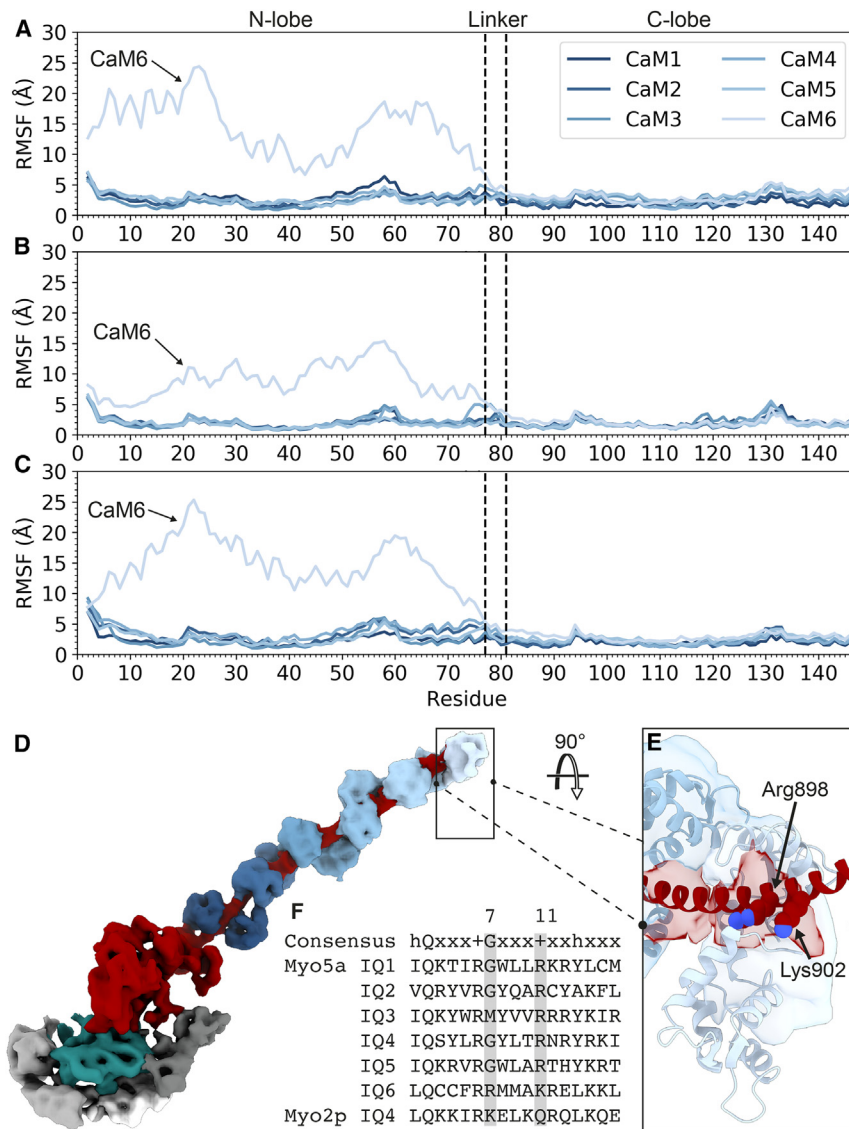


Figure 2. Variation in CaM interaction with IQ1-6 along the length of the lever

(A-C) Plots of per residue RMSF (root-mean-square Fluctuation) of CaMs obtained from 3 individual pseudoatomic model simulations in which the heavy chain is restrained, and the CaMs are unrestrained. The locations of the N-lobe, linker and C-lobe are indicated. (A-C) show the results for these individual repeats. RMSF was calculated in CPPTRAJ (C++ Process Trajectory).³⁶

(D) Cryo-EM map of Myo5a S1 demonstrating the weak density for the N-lobe of CaM bound to IQ6 (CaM6) boxed.

(E) 90° rotation of boxed region in (D), with a pseudoatomic model fitted to the cryo-EM density. Residues at positions 7 (Arg898) and 11 (Lys902) of IQ6 are displayed in sphere mode and labeled.

(F) Sequence alignment of all 6 IQ motifs of murine Myo5a together with IQ4 of Myo2p (PDB: 1M46¹⁹). Positions 7 and 11 of each IQ motif are highlighted in gray.

The lever of Myo5A is composed of 6 CaM IQ motifs that alternate in length from 23 residues (IQ1, 3, and 5) to 25 residues (IQ2, 4, and 6). In the pseudoatomic model, we found that the conformation of the CaM bound to the shorter IQ motifs (1, 3, and 5) was highly similar (Figure S4A). Likewise, CaM bound to the longer IQ motifs (2 and 4) was also similar. However, as indicated by the cryo-EM density, the N-lobe of CaM6 (CaM bound to IQ6) only weakly interacts with the IQ motif (Figure S4B) and is poorly resolved (Figures 1C, 2D, and 2E). Interestingly, unlike IQ6, the substitution of Gly7 with Met in IQ3 does not result in an extended conformation in the bound CaM, as density for both lobes can be seen in the cryo-EM density map (Figures 2D, 2F, and S4A). Moreover, previous work

showed that the interaction of the motor with F-actin is relatively invariant.

The cryo-EM density for the class with the highest overall resolution (class *d*; Figure 1B) was fit with a pseudoatomic model (Figure 1C), using all-atom molecular dynamics (MD) simulations to determine the arrangement of the bound CaMs and their interactions within the lever. The heavy chain was restrained, and the CaMs were unrestrained in these simulations. The cryo-EM density for the N-lobe of CaM bound to the 6th IQ motif (CaM6) is poorly resolved. It has been predicted that the CaM bound to IQ6 would adopt an extended conformation, with its N-lobe extending away from the IQ motif, due to the substitution of Gly7 with Arg (Figure 2F).^{17,18} Thus, in the pseudoatomic model, we used the extended light chain conformation of MLC1P bound to IQ4 in the yeast myosin-5 Myo2p crystal structure (PDB: 1M46¹⁹) to build in CaM6. Our pseudoatomic model also included the C-terminal FLAG tag sequence (DYKDDDDK) in the heavy chain, present after IQ6 (residue 908 onwards).

showed that the Gly7Met substitution in a consensus IQ motif (AATK/QAAFRGHITRKKLK) weakened its interaction with CaM by ~10-fold.¹⁷ In the full-length intact lever, it is likely that neighboring CaMs reduce the flexibility of the N-lobe of CaM3, stabilizing its interactions with the IQ motif, suggesting CaMs bind the heavy chain cooperatively. Various studies have identified that Ca²⁺ affects CaM binding to the lever, with CaM2 being the most sensitive to Ca²⁺,²⁰ IQ2 having the weakest affinity for CaM²¹ and CaM2 most likely to dissociate from the lever when Ca²⁺ increases.^{20,22} The loss of CaM2, and its stabilizing interactions with CaM3, may result in the extension of the N-lobe of CaM3, which in turn could contribute to the destabilization of the lever at increased Ca²⁺ levels.

Comparing the mobility of CaM6 to the other 5 CaMs using MD simulations demonstrated that the extended conformation of its N-lobe (Figure S4B) is more mobile and does not tend toward the canonical closed state (Figures 2A-2C). The increased mobility of the N-lobe of CaM6 compared to CaMs 1-5, is consistent

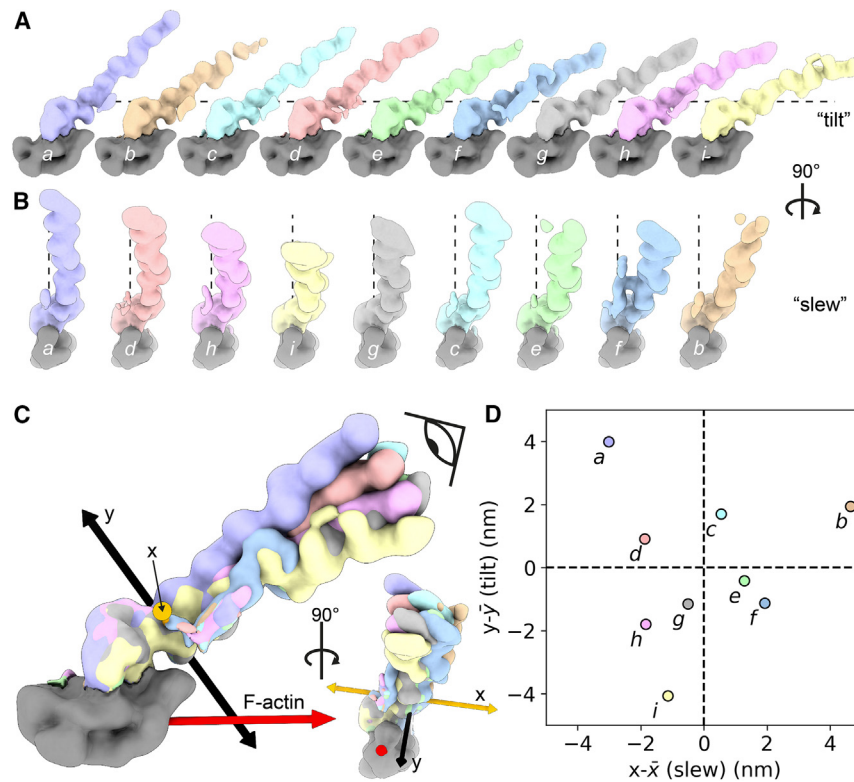


Figure 3. The overall bending stiffness of the lever is directionally isotropic within cryo-EM 3D classes

(A) Post-processed maps of cryo-EM 3D classes in order of lever bend along the F-actin longitudinal axis (tilt). Visualized in the xy plane of the maps. The dashed line parallel to the x axis of the maps emphasizes the change lever bend between classes. Maps are Gaussian smoothed (SD 5 Å) (contour level: 0.15).

(B) Post-processed maps of cryo-EM 3D classes in order of lever bend along the F-actin short axis (slew). Visualized in the zy plane of the maps. The dashed line parallel to the y axis of the maps emphasizes the change lever bend between classes.

(C) Post-processed maps of cryo-EM 3D classes overlaid. The coordinate systems the cantilever bending stiffness measurements were taken from are displayed as 3D arrows (see STAR Methods). x axis = orange arrows, y axis = black arrows, z = axis mean lever vector (see STAR Methods). Eye shows viewpoint graphed in (D).

(D) Plot of the displacement of the end of the lever in each class from the mean (z) (see STAR Methods), used to calculate the overall bending stiffness. Changes in x represent motion across the F-actin short axis (slew), changes in y represent tilt motions toward and away from the F-actin longitudinal axis (tilt).

with its weak density in the cryo-EM map (Figure 2D). The mobility of the C-lobe was similar for all CaMs. However, we cannot entirely rule out that in our Myo5a S1 construct, the lack of downstream sequence is partly responsible for weaker interactions between the N-lobe of CaM and IQ6 compared to the full-length motor. Interestingly, the recent shutdown structure of full-length Myo5a shows all 6 IQ-CaM interactions are conserved; however, the N-lobe of CaM6 is in close contact with one of α -helical strands of the coiled coil, stabilizing the sharp bend at the head-tail junction.²³ This is consistent with the idea that the N-lobe of CaM6 is more mobile as conformational changes occur at this region during switching between the shutdown and active state. On balance, we think it is likely that the interaction between the N-lobe of CaM and IQ6 is labile, which may be important for helping the switch between the shutdown and active state, and that the N-lobes of CaMs bound to IQ3 and IQ6 can extend into the solvent, as reported for Mlc1p and Myo2p at IQ4,¹⁹ if upstream or downstream stabilizing interactions between adjacent CaMs are absent.

The flexural rigidity of the Myo5a lever varies along its length

The decrease in local resolution along the lever and the 9 different lever positions in the 3D classes, demonstrate the intrinsic flexibility of the lever, unconfined by a second head. Using the 3D classes, we calculated the overall bending stiffness of the lever, by measuring the difference in position of the distal end of the lever in each 3D cryo-EM class from the mean position when the converter is superposed (Figures 3 and S5A) (see STAR Methods for details). We define the start

of our lever as the converter and the end as the midpoint along the CaM bound to IQ6. Of note, although the decrease in resolution toward the end of the lever results in some uncertainty about the position of CaM6, excluding it would artificially reduce the length of the lever and would therefore make the bending stiffness appear higher. The bending stiffness increases as the cube of the lever length, thus a 15% reduction in the lever length would increase the stiffness by 60%. However, the flexural rigidity of this section is less significant to the determination of the displacement (the contribution is proportional to the square of the distance from the free end) than sections that are closer to the motor domain.

Treating the lever of Myo5a as a cantilever, we calculated its overall bending stiffness to be $0.75 \pm 0.07 \text{ pN nm}^{-1}$ for Myo5a. The bending stiffness is directionally isotropic, as the calculated values for slew (across F-actin short axis) and tilt (bending toward and away from F-actin) are not significantly different (0.77 pN nm^{-1} and 0.73 pN nm^{-1} , respectively [$\pm 0.3 \text{ pN nm}^{-1}$ confidence interval]) (Figures 3 and S5C), and the covariance is small compared to the variance (Pearson's correlation coefficient is 0.02). The overall variation in the angle of twist over the whole lever is $\sim \pm 20^\circ$. This is sufficiently small to be ignored in terms of mixing between the motions of slew and tilt. Furthermore, as the bending stiffness is isotropic, twisting does not affect bending. If we additionally include the motor in this calculation, using the base as the start point of our lever (Figure S6), the bending stiffness for the head in rigor is 0.67 pN nm^{-1} . Our estimates of the overall bending stiffness are similar in magnitude to that recently determined for the full Myo5a head using negative stain EM (ns-EM) (0.75 pN nm^{-1}),²⁴ and to previous estimates

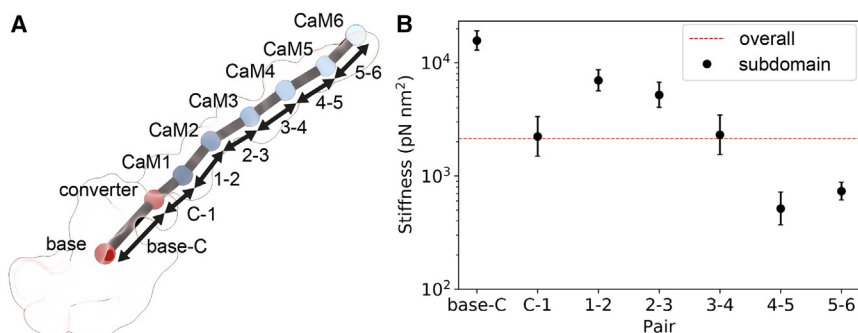


Figure 4. Determining the local flexural rigidity of lever subdomains from the cryo-EM data

(A) An example discretization of Myo5a S1 (class *d*) into 7 subdomains for calculating the local flexural rigidity (see STAR Methods for details), displayed within the Gaussian smoothed cryo-EM map (SD 5 Å) (contour level: 0.15).

(B) The calculated local flexural rigidity for subdomains of Myo5a S1 (A). The flexural rigidity of a uniform beam corresponding to the overall lever bending stiffness is plotted as a red line (overall). Base = F-actin binding interface, C = converter, 1 = CaM1, 2 = CaM2, 3 = CaM4, 5 = CaM5, 6 = CaM6. Error bars show the SD of the random error (see STAR Methods for details) as a percentage of the reported stiffness. See also Table S1.

from optical trap measurements (0.2 pN nm^{-12}), and ns-EM images of dimeric actomyosin-5a ($0.26 \text{ pN nm}^{-125}$).

The overall bending stiffness of the lever can then be used to calculate the maximum deflection of the lever when forces of a similar magnitude to those experienced by Myo5a are applied to its end. For example, the intramolecular strain across the dimer when both heads are bound has been calculated to be 2 pN .¹⁴ The stall force for Myo5a dimers walking along F-actin in an optical trap assay has been calculated to be $\sim 3 \text{ pN}$,⁸ and the stall force for a monomer bound to F-actin to be $\sim 4 \text{ pN}$.²⁶ For an overall bending stiffness of 0.75 pN nm^{-1} , we calculate that the lever would be deflected by $1.5\text{--}3.0 \text{ nm}$ across this force range, which corresponds to $0.9\text{--}1.7 \text{ nm}$ along F-actin (STAR Methods). Interestingly, the 4 pN force would deflect the lever close to the limit of the unstrained fluctuations we observe ($\sim 4 \text{ nm}$) (Figure 3D). The lever deflections in this force range are approximately equivalent to the change in lever end distance between the rigor and ADP state. This could explain how forces in this range alter lever position sufficiently to prevent entry into the rigor state. Note that deflections close to motor will be much smaller, $0.04\text{--}0.09 \text{ nm}$ for CaM1 ($0.03\text{--}0.05 \text{ nm}$ along F-actin).

The density for all 6 CaMs in our 3D classes further allows us to determine if the lever behaves as a beam with uniform bending or if there are distinct points of flexion along its length. These are thought to arise from increased spacing and reduction in CaM-CaM interactions between a CaM bound to an IQ motif that is 25 residues long and its neighboring C-terminal IQ motif, 23 residues long, such as IQ2 and IQ3.¹⁸ A further pliant region could also lie between the converter and the CaM bound to IQ1 (CaM1).^{13,27}

To quantify the variation in flexural rigidity along the lever we first discretized Myo5a into 7 subdomains (Figures 4A and S6A) and then used the variance in subdomain conformations captured in the cryo-EM 3D classes (Figures S6C–S6E and S7A–S7C) to calculate the flexural rigidity of each subdomain. The resulting values (Figures 4B and S6F; Table S1) can be compared to the flexural rigidity of a uniform beam, where a bending stiffness (0.75 pN nm^{-1}) for a lever of 20.4 nm (the average distance between the midpoint of CaM bound to IQ6 and the converter) gives a flexural rigidity (EI) of $2,100 \text{ pN nm}^2$ (dotted red line, Figure 4B). This is similar to the value estimated previously ($EI = 1,500 \text{ pN nm}^2$) from the force a lever bears under conditions close to stall.²⁸

The flexural rigidities calculated from our cryo-EM data (Figure 4B; Table S1) suggest that stiffness is not uniform but varies along the length of the lever. As anticipated, one of the regions of increased pliancy is the “pliant point” between the converter and CaM1,^{13,27} which has a flexural rigidity similar to that expected for a uniform beam. Of note, the flexural rigidity here is more than a factor of 3 smaller than the neighboring regions and is strongly anisotropic. Thereafter, the regions between each IQ range in stiffness from stiffer than a uniform beam (IQ1–2 and 2–3), to equally as stiff (IQ3–4) and less stiff (IQ 4–5 and 5–6) (Figure 4B). Our data suggest that the variation in IQ spacings and CaM-CaM interactions do not dictate the stiffness at subdomains in contrast to earlier predictions.¹⁸ Moreover, flexural rigidity (Figures 4B and S6F; Table S1) is not correlated with subdomain pair conformation as measured by angular distribution (Figures S7A–S7C), distance (Figure S7D) or interdomain interactions. Of note, subdomain pair conformation measurements from previously obtained structures fall within a similar range to our measurements (Figure S7). Finally, if Myo5a acts as a cantilever, the moment (tendency of a force to cause bending about the hinge) at each point along the lever is proportional to its distance from where the force is being applied. Thus, if there are indeed regions of pliancy along the length of the lever then the effects of forces on these regions will be most strongly felt the further away from the cantilever end and the closer to the opposing force of the fixed end they are. This may explain why only the region between the converter and CaM1 has been the previously identified as pliant, as previous EM analysis was performed on the double head bound dimer as opposed to an unrestrained lever considered here.

The change in flexural rigidity along the length of the lever is likely to be important for Myo5a mechanics. The lever must be sufficiently stiff to generate intramolecular strain and to withstand load from cargos without collapsing. The lever must also be sufficiently flexible to accommodate changes in step size, stereospecific binding to F-actin, and swapping filament track in an F-actin network.^{25,29} A Myo5a construct that comprises two IQ domains followed by a single alpha helix (SAH), which replaces IQ domains 3–6, can still walk processively, but does not generate intramolecular strain.³⁰ The flexural rigidity of an SAH is $\sim 150 \text{ pN nm}^2$ which is $\sim 1/4$ the stiffness between CaM4–6 ($520 \pm 200 \text{ pN nm}^2$ at the CaM4–5 subdomain, and $730 \pm 150 \text{ pN nm}^2$ at the CaM5–6 subdomain). Taken together this could

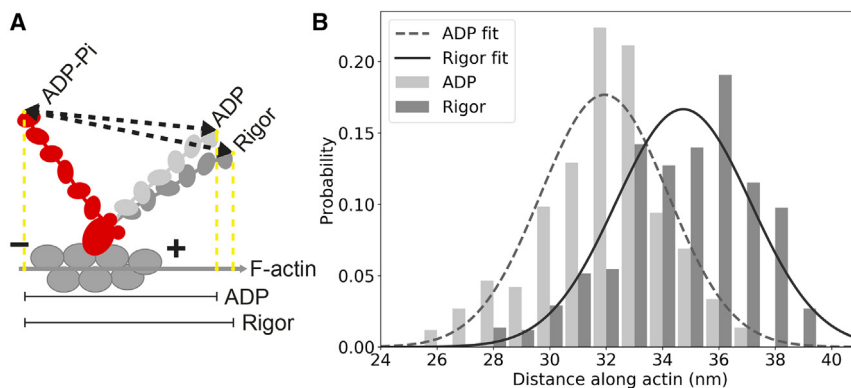


Figure 5. The working stroke of Myo5a is 35 nm

(A) Schematic diagram to demonstrate how distances for (B) were calculated. Distances between lever ends in the modeled ADP-P_i, ADP, and rigor conformations (see [Figure S8](#) and [STAR Methods](#) for details) are shown as black dashed arrows. Yellow dashed lines show these distances as a translation along the F-actin vector (0th to 13th subunit, gray arrow, see [STAR Methods](#) for details). + indicates the plus end of F-actin, – indicates the minus end of F-actin.

(B) Histogram of the translation of Myo5a lever ends along F-actin vector from the ADP-P_i conformation to ADP and to rigor (see [STAR Methods](#) for details), and the fitted Gaussian distributions. The probability of each class being paired was calculated using the proportion of particles in each of the cryo-EM 3D classes (see [STAR Methods](#)).

mean that some rigidity at the start of the lever is required for transmitting the powerstroke and some rigidity (at least $4 \times$ SAH stiffness) is required to communicate intramolecular strain between heads. The flexibility toward the end of the lever may help accommodate for stepping errors and angular disorder in F-actin.²⁴

Lever flexibility augments Myo5a working stroke

The working stroke is considered to result from small conformational changes in the motor domain, resulting from P_i and ADP release, that are amplified by a large movement of the lever. However, as our data show, rather than a single conformation for the lever in the rigor (post-powerstroke) state, a range of lever conformations is possible. If we assume a similar range of lever conformations is possible in the ADP-P_i (pre-powerstroke) state, then we can use this to calculate the range of possible values for the working stroke.

First, we determined the range of lever end positions for the rigor state by flexibly fitting the lever model of class *d* into each of the 3D classes (*a–i*, [Figure 1A](#)) ([STAR Methods](#)). We chose the end of the lever to be residue 912 (res 912 C α atom), the last residue that is likely to interact with CaM in the active dimer. This residue was selected as it is the last interacting residue for CaM bound to IQ2 in the IQ1–2 crystal structure (PDB: 2IX7³¹). Although density for the N-lobe of CaM6 is lacking, we expect that it would interact with the heavy chain in the dimer, as observed in the shutdown state.²³ As there is no deposited structure of the F-actin bound ADP-P_i motor, it was necessary to generate a model. Thus, we used the structure of Myo5a bound to an ADP-P_i analog (ADP-VO₄) (PDB: 4ZG4³²) and modeled the F-actin bound state by docking residues 490–530 of the ADP-VO₄ structure (PDB: 4ZG4³²) onto residues 492–532 of ADP F-actin bound structure (PDB: 7PM6) ([Figure S8](#)). This method of docking was chosen as the L50 domain interaction with F-actin has recently been shown to be conserved in the ADP and ADP-P_i bound state.³³ To model the range of lever end positions for the ADP-P_i and ADP states we then superimposed our lever models for each of the 3D classes onto the converter domains of our ADP-P_i model, and the recent Myo5a-ADP structure bound to F-actin (PDB: 7PM5¹⁶) ([Figure S8](#)). Finally, we determined the distance traveled along the F-actin longitudinal

axis between each nucleotide state for all combinations of lever conformations ([Figures 5A](#) and [S8](#)).

Using this approach, we calculate the working stroke of Myo5a (between the ADP-P_i and rigor state) to be 35 ± 6 nm (mean \pm standard deviation [SD], [Figure 5](#)). The translation between the ADP-P_i and ADP states is 3 nm shorter (32 ± 5 nm [mean \pm SD]) ([Figures 5](#) and [S8](#)), consistent with the known structural transition of Myo5a on ADP release.¹⁶ Incidentally, if we superimpose the model of the lever for each 3D class on CaM1 instead, to account for potential increased interactions of CaM1 with the converter and motor in the pre-powerstroke state, the estimated working stroke only increases by 1 nm. Moreover, the distribution of working strokes we observe ([Figure 5B](#)) could help to account for the variation in step size recently demonstrated for the Myo5a dimer using high-resolution interferometric scattering microscopy.²⁴

The value we determine for the working stroke is similar to that calculated in a recent cryo-EM study that used a Myo5a S1 (single IQ) mutant, in which product release following hydrolysis is slow.³³ In that study the lever from the shutdown state structure²³ was superimposed onto their pre- and post-powerstroke structures bound to F-actin to calculate a powerstroke of 34 nm. Both of these two new estimates of the working stroke are higher than previous reports. In one earlier study, the working stroke was estimated to be 27 nm using structures of Myo5a S1 (single IQ) in F-actin bound ADP and rigor states, the ADP-VO₄ structure, and modeling in the full-length lever.³² Our higher estimate can be accounted for by the use of a model that more accurately represents the F-actin bound ADP-P_i state³³ and the use of a population of flexible levers rather than a single straight lever. Previous estimates obtained from optical trap measurements were 25 nm for dimeric Myo5a and 21 nm for Myo5a S1.¹² However, these estimates may be biased to preferentially select smaller displacements than the working stroke.³⁴

Our larger estimate of the working stroke suggests that the diffusive search a newly detached myosin head needs to perform to rebind to F-actin at the next binding site in the walking dimer, is closer to 1 nm and not ~ 10 nm as previously suggested.¹² Instead, the length of the working stroke of a single head is sufficient to translate the molecule by ~ 35 nm, which is close to the ~ 36 nm helical F-actin repeat. This raises the

idea that strain across the dimeric molecule is not generated during binding of the new lead head but is only generated after P_i release. Strain therefore arises from the trail head preventing the lead head from entering the post-powerstroke state, as originally suggested from ns-EM images of Myo5a walking along actin.³⁵

CONCLUSION

3D reconstruction of the full-length Myo5a lever domain in 9 different conformations has revealed properties of the lever that contribute to its mechanics. Analyzing the overall bending stiffness demonstrates that the stiffness of the lever is directionally isotropic. This means that the lever can accommodate intramolecular strain in a walking dimeric motor in all directions as it navigates a complex F-actin network. Analyzing the flexural rigidity along the length of the lever has shown its stiffness is not uniform but varies along its length, with the first pliant region between the converter and CaM1 and further pliant regions beyond IQ3. The initial region of the lever, comprising IQs 1–3 and their associated CaMs, is relatively stiff compared to the end of the lever. Interestingly, no single characteristic, i.e., the conformation of the subdomain or the number of interdomain interactions seems to correlate with flexural rigidity. This suggests that either the combined influence of these features encodes the flexural rigidity at subdomains or features yet unexplored.

3D cryo-EM reconstruction is an important approach in estimating bending stiffnesses and can provide a more direct analysis than other techniques. Due to 3D resolution along the length of the lever we were able to probe properties of the lever directly. The variable flexibility along the length of the lever demonstrated here challenges previous hypotheses that assume the lever is a beam with uniform bending along its length. It is possible that images of the dimer with both heads bound to F-actin under strain have led to this idea, as they show a taut lever as opposed to one that can flex and bend (e.g., a tightrope is rigid under strain but is made of flexible rope), which prevents different properties along the length of the lever from being revealed. This highlights the value of using a single head as the lever is not constrained.

The ensemble of lever conformations within the cryo-EM 3D classes has further allowed us to calculate a working stroke that is longer than previously described,^{12,32} and that strain between the two attached heads in the walking motor is likely to only be generated once the motor has bound to F-actin, and P_i has been released. The nature of this strain, and its effect on the structure of the lead and trail heads will require cryo-EM structures of the Myo5a dimer as it walks along actin, a key challenge for the future.

RESOURCE AVAILABILITY

Lead contact

Further information and requests for resources and reagents should be directed to and will be fulfilled by the lead contact, Michelle Peckham (m.peckham@leeds.ac.uk).

Materials availability

This study did not generate new unique reagents.

Data and code availability

- The EM density maps for the nine 3D class reconstructions (class *a* [EMDB: EMD-16846], class *b* [EMDB: EMD-16848], class *c* [EMDB: EMD-16849], class *d* [EMDB: EMD-16850], class *e* [EMDB: EMD-16851], class *f* [EMDB: EMD-16853], class *g* [EMDB: EMD-16852], class *h* [EMDB: EMD-16854], and class *i* [EMDB: EMD-16855]), and the reconstruction focused on the motor domain with the first two IQs only (EMDB: EMD-16856), have been deposited in EMDB. The simulated pseudoatomic model for class *d* was deposited in the PDB (PDB: 8OF8). They are publicly available as of the date of publication.
- This paper does not report original code.
- Any additional information required to reanalyze the data reported in this paper is available from the [lead contact](#) upon request.

ACKNOWLEDGMENTS

We would like to thank Eva Forgacs, Betty Virok and Howard White for the generous gift of purified Myo5a S1 protein. We would like to thank Glenn Carrington, Peter J. Knight and Yasuharu Takagi for the helpful discussion and advice. We would like to thank the Astbury Biostructure Laboratory for their support. The FEI Titan Krios microscopes were funded by the University of Leeds (JoL ABSL award) and Wellcome Trust (108466/Z/15/Z). This work made use of the facilities of the N8 Center of Excellence in Computationally Intensive Research (N8 CIR) provided and funded by the N8 research partnership and EPSRC (EP/T022167/1), through HECBioSim (EP/R013012). The center is coordinated by the Universities of Durham, Manchester and York, UK. This work was also undertaken on ARC4, part of the High-Performance Computing facilities at the University of Leeds, UK. M.S.C.G. and D.P.K. were PhD students on the Wellcome Trust 4-year PhD program (102174/B/13/Z) in The Astbury Center funded by The University of Leeds. M.P. is funded by the Wellcome Trust Investigator award “Myosin structure and regulation” (223125/Z/21/Z). We would also like to thank Emily S. Brown for her help designing the graphical abstract.

AUTHOR CONTRIBUTIONS

Conceptualization: M.S.C.G., S.A.H., S.P.M., and M.P. Methodology: M.S.C.G., D.P.K., O.G.H., D.J.R., S.A.H., S.P.M., and M.P. Investigation: M.S.C.G. Supervision: S.A.H., S.P.M., and M.P. Writing – original draft: M.S.C.G., M.P., S.P.M., and S.A.H. Writing – review & editing: M.S.C.G., D.P.K., O.G.H., D.J.R., S.A.H., S.P.M., and M.P.

DECLARATION OF INTERESTS

The authors declare no competing interests.

STAR★METHODS

Detailed methods are provided in the online version of this paper and include the following:

- [KEY RESOURCES TABLE](#)
- [EXPERIMENTAL MODEL AND STUDY PARTICIPANT DETAILS](#)
- [METHOD DETAILS](#)
 - Sample preparation
 - Grid preparation and cryo-EM data acquisition
 - Cryo-EM image processing
 - Cryo-EM model building and refinement
 - Flexibility analysis
 - Predicting the working stroke
- [QUANTIFICATION AND STATISTICAL ANALYSIS](#)

SUPPLEMENTAL INFORMATION

Supplemental information can be found online at <https://doi.org/10.1016/j.str.2024.09.025>.

Received: February 22, 2024
Revised: July 9, 2024
Accepted: September 30, 2024
Published: October 24, 2024

REFERENCES

- Foth, B.J., Goedecke, M.C., and Soldati, D. (2006). New insights into myosin evolution and classification. *Proc. Natl. Acad. Sci. USA* *103*, 3681–3686. <https://doi.org/10.1073/pnas.0506307103>.
- Hartman, M.A., and Spudich, J.A. (2012). The myosin superfamily at a glance. *J. Cell Sci.* *125*, 1627–1632. <https://doi.org/10.1242/jcs.094300>.
- Kollmar, M., and Mülhhausen, S. (2017). Myosin repertoire expansion coincides with eukaryotic diversification in the Mesoproterozoic era. *BMC Evol. Biol.* *17*, 211. <https://doi.org/10.1186/s12862-017-1056-2>.
- Bustamante, C., Keller, D., and Oster, G. (2001). The physics of molecular motors. *Acc. Chem. Res.* *34*, 412–420. <https://doi.org/10.1021/ar0001719>.
- Purcell, E.M. (1977). Life at low Reynolds number. *Am. J. Phys.* *45*, 3–11. <https://doi.org/10.1119/1.10903>.
- Cheney, R.E., O’Shea, M.K., Heuser, J.E., Coelho, M.V., Wolenski, J.S., Espreefaco, E.M., Forscher, P., Larson, R.E., and Mooseker, M.S. (1993). Brain myosin-V is a two-headed unconventional myosin with motor activity. *Cell* *75*, 13–23.
- De La Cruz, E.M., and Ostap, E.M. (2004). Relating biochemistry and function in the myosin superfamily. *Curr. Opin. Cell Biol.* *16*, 61–67. <https://doi.org/10.1016/j.ceb.2003.11.011>.
- Mehta, A.D., Rock, R.S., Rief, M., Spudich, J.A., Mooseker, M.S., and Cheney, R.E. (1999). Myosin-V is a processive actin-based motor. *Nature* *400*, 590–593. <https://doi.org/10.1038/23072>.
- Rief, M., Rock, R.S., Mehta, A.D., Mooseker, M.S., Cheney, R.E., and Spudich, J.A. (2000). Myosin-V stepping kinetics: a molecular model for processivity. *Proc. Natl. Acad. Sci. USA* *97*, 9482–9486. <https://doi.org/10.1073/pnas.97.17.9482>.
- Sakamoto, T., Wang, F., Schmitz, S., Xu, Y., Xu, Q., Molloy, J.E., Veigel, C., and Sellers, J.R. (2003). Neck length and processivity of myosin V. *J. Biol. Chem.* *278*, 29201–29207. <https://doi.org/10.1074/jbc.M303662200>.
- De La Cruz, E.M., Wells, A.L., Rosenfeld, S.S., Ostap, E.M., and Sweeney, H.L. (1999). The kinetic mechanism of myosin V. *Proc. Natl. Acad. Sci. USA* *96*, 13726–13731. <https://doi.org/10.1073/pnas.96.24.13726>.
- Veigel, C., Wang, F., Bartoo, M.L., Sellers, J.R., and Molloy, J.E. (2002). The gated gait of the processive molecular motor, myosin V. *Nat. Cell Biol.* *4*, 59–65. <https://doi.org/10.1038/ncb732>.
- Burgess, S., Walker, M., Wang, F., Sellers, J.R., White, H.D., Knight, P.J., and Trinick, J. (2002). The prepower stroke conformation of myosin V. *J. Cell Biol.* *159*, 983–991. <https://doi.org/10.1083/jcb.200208172>.
- Oguchi, Y., Mikhailenko, S.V., Ohki, T., Olivares, A.O., De La Cruz, E.M., and Ishiwata, S. (2008). Load-dependent ADP binding to myosins V and VI: implications for subunit coordination and function. *Proc. Natl. Acad. Sci. USA* *105*, 7714–7719. <https://doi.org/10.1073/pnas.0800564105>.
- Forgacs, E., Cartwright, S., Sakamoto, T., Sellers, J.R., Corrie, J.E.T., Webb, M.R., and White, H.D. (2008). Kinetics of ADP dissociation from the trail and lead heads of actomyosin V following the power stroke. *J. Biol. Chem.* *283*, 766–773. <https://doi.org/10.1074/jbc.M704313200>.
- Pospich, S., Sweeney, H.L., Houdusse, A., and Raunser, S. (2021). High-resolution structures of the actomyosin-V complex in three nucleotide states provide insights into the force generation mechanism. *Elife* *10*, e73724. <https://doi.org/10.7554/eLife.73724>.
- Black, D.J., and Persechini, A. (2010). Variations at the semiconserved glycine in the IQ domain consensus sequence have a major impact on Ca²⁺-dependent switching in calmodulin-IQ domain complexes. *Biochemistry* *49*, 78–83. <https://doi.org/10.1021/bi901695p>.
- Terrak, M., Rebowksi, G., Lu, R.C., Grabarek, Z., and Dominguez, R. (2005). Structure of the light chain-binding domain of myosin V. *Proc. Natl. Acad. Sci. USA* *102*, 12718–12723. <https://doi.org/10.1073/pnas.0503899102>.
- Terrak, M., Wu, G., Stafford, W.F., Lu, R.C., and Dominguez, R. (2003). Two distinct myosin light chain structures are induced by specific variations within the bound IQ motifs-functional implications. *EMBO J.* *22*, 362–371. <https://doi.org/10.1093/emboj/cdg058>.
- Trybus, K.M., Gushchin, M.I., Lui, H., Hazelwood, L., Kremetsova, E.B., Volkman, N., and Hanein, D. (2007). Effect of calcium on calmodulin bound to the IQ motifs of myosin V. *J. Biol. Chem.* *282*, 23316–23325. <https://doi.org/10.1074/jbc.M701636200>.
- Martin, S.R., and Bayley, P.M. (2004). Calmodulin bridging of IQ motifs in myosin-V. *FEBS Lett.* *567*, 166–170. <https://doi.org/10.1016/j.febslet.2004.04.053>.
- Shen, M., Zhang, N., Zheng, S., Zhang, W.B., Zhang, H.M., Lu, Z., Su, Q.P., Sun, Y., Ye, K., and Li, X.D. (2016). Calmodulin in complex with the first IQ motif of myosin-5a functions as an intact calcium sensor. *Proc. Natl. Acad. Sci. USA* *113*, E5812–E5820. <https://doi.org/10.1073/pnas.1607702113>.
- Niu, F., Liu, Y., Sun, K., Xu, S., Dong, J., Yu, C., Yan, K., and Wei, Z. (2022). Autoinhibition and activation mechanisms revealed by the triangular-shaped structure of myosin Va. *Sci. Adv.* *8*, eadd4187. <https://doi.org/10.1126/sciadv.add4187>.
- Fineberg, A., Takagi, Y., Thirumurugan, K., Andrecka, J., Billington, N., Young, G., Cole, D., Burgess, S.A., Curd, A.P., Hammer, J.A., et al. (2024). Myosin-5 varies its step length to carry cargo straight along the irregular F-actin track. *Proc. Natl. Acad. Sci. USA* *121*, e2401625121. <https://doi.org/10.1073/pnas.2401625121>.
- Oke, O.A., Burgess, S.A., Forgacs, E., Knight, P.J., Sakamoto, T., Sellers, J.R., White, H., and Trinick, J. (2010). Influence of lever structure on myosin 5a walking. *Proc. Natl. Acad. Sci. USA* *107*, 2509–2514. <https://doi.org/10.1073/pnas.0906907107>.
- Sellers, J.R., and Veigel, C. (2010). Direct observation of the myosin-Va power stroke and its reversal. *Nat. Struct. Mol. Biol.* *17*, 590–595. <https://doi.org/10.1038/nsmb.1820>.
- Houdusse, A., Szent-Gyorgyi, A.G., and Cohen, C. (2000). Three conformational states of scallop myosin S1. *Proc. Natl. Acad. Sci. USA* *97*, 11238–11243. <https://doi.org/10.1073/pnas.200376897>.
- Vilfan, A. (2005). Elastic lever-arm model for myosin V. *Biophys. J.* *88*, 3792–3805. <https://doi.org/10.1529/biophysj.104.046763>.
- Lombardo, A.T., Nelson, S.R., Kennedy, G.G., Trybus, K.M., Walcott, S., and Warshaw, D.M. (2019). Myosin Va transport of liposomes in three-dimensional actin networks is modulated by actin filament density, position, and polarity. *Proc. Natl. Acad. Sci. USA* *116*, 8326–8335. <https://doi.org/10.1073/pnas.1901176116>.
- Baboolal, T.G., Sakamoto, T., Forgacs, E., White, H.D., Jackson, S.M., Takagi, Y., Farrow, R.E., Molloy, J.E., Knight, P.J., Sellers, J.R., and Peckham, M. (2009). The SAH domain extends the functional length of the myosin lever. *Proc. Natl. Acad. Sci. USA* *106*, 22193–22198. <https://doi.org/10.1073/pnas.0909851106>.
- Houdusse, A., Gaucher, J.F., Kremetsova, E., Mui, S., Trybus, K.M., and Cohen, C. (2006). Crystal structure of apo-calmodulin bound to the first two IQ motifs of myosin V reveals essential recognition features. *Proc. Natl. Acad. Sci. USA* *103*, 19326–19331. <https://doi.org/10.1073/pnas.0609436103>.
- Wulf, S.F., Ropars, V., Fujita-Becker, S., Oster, M., Hofhaus, G., Trabuco, L.G., Pylypenko, O., Sweeney, H.L., Houdusse, A.M., and Schröder, R.R. (2016). Force-producing ADP state of myosin bound to actin. *Proc. Natl. Acad. Sci. USA* *113*, E1844–E1852. <https://doi.org/10.1073/pnas.1516598113>.
- Klebl, D.P., McMillan, S.N., Risi, C., Forgacs, E., Virok, B., Atherton, J.L., Stofella, M., Winkelmann, D.A., Sobott, F., Galkin, V.E., et al. (2024). Swinging lever mechanism of myosin directly demonstrated by time-resolved cryoEM. Preprint at bioRxiv. <https://doi.org/10.1101/2024.01.05.574365>.

34. Sleep, J., Lewalle, A., and Smith, D. (2006). Reconciling the working strokes of a single head of skeletal muscle myosin estimated from laser-trap experiments and crystal structures. *Proc. Natl. Acad. Sci. USA* *103*, 1278–1282. <https://doi.org/10.1073/pnas.0506272103>.
35. Walker, M.L., Burgess, S.A., Sellers, J.R., Wang, F., Hammer, J.A., 3rd, Trinick, J., and Knight, P.J. (2000). Two-headed binding of a processive myosin to F-actin. *Nature* *405*, 804–807. <https://doi.org/10.1038/35015592>.
36. Roe, D.R., and Cheatham, T.E., 3rd (2013). PTRAJ and CPPTRAJ: Software for Processing and Analysis of Molecular Dynamics Trajectory Data. *J. Chem. Theor. Comput.* *9*, 3084–3095. <https://doi.org/10.1021/ct400341p>.
37. Forgacs, E., Cartwright, S., Kovács, M., Sakamoto, T., Sellers, J.R., Corrie, J.E.T., Webb, M.R., and White, H.D. (2006). Kinetic mechanism of myosinV-S1 using a new fluorescent ATP analogue. *Biochemistry* *45*, 13035–13045. <https://doi.org/10.1021/bi060712n>.
38. Wang, F., Chen, L., Arcucci, O., Harvey, E.V., Bowers, B., Xu, Y., Hammer, J.A., 3rd, and Sellers, J.R. (2000). Effect of ADP and ionic strength on the kinetic and motile properties of recombinant mouse myosin V. *J. Biol. Chem.* *275*, 4329–4335. <https://doi.org/10.1074/jbc.275.6.4329>.
39. Pardee, J.D., and Spudich, J.A. (1982). Purification of muscle actin. *Methods Enzymol.* *85 Pt B*, 164–181. [https://doi.org/10.1016/0076-6879\(82\)85020-9](https://doi.org/10.1016/0076-6879(82)85020-9).
40. Zheng, S.Q., Palovcak, E., Armache, J.P., Verba, K.A., Cheng, Y., and Agard, D.A. (2017). MotionCor2: anisotropic correction of beam-induced motion for improved cryo-electron microscopy. *Nat. Methods* *14*, 331–332. <https://doi.org/10.1038/nmeth.4193>.
41. Zhang, K. (2016). Gctf: Real-time CTF determination and correction. *J. Struct. Biol.* *193*, 1–12. <https://doi.org/10.1016/j.jsb.2015.11.003>.
42. Zivanov, J., Nakane, T., Forsberg, B.O., Kimanius, D., Hagen, W.J., Lindahl, E., and Scheres, S.H. (2018). New tools for automated high-resolution cryo-EM structure determination in RELION-3. *Elife* *7*, e42166. <https://doi.org/10.7554/eLife.42166>.
43. Pettersen, E.F., Goddard, T.D., Huang, C.C., Couch, G.S., Greenblatt, D.M., Meng, E.C., and Ferrin, T.E. (2004). UCSF Chimera—a visualization system for exploratory research and analysis. *J. Comput. Chem.* *25*, 1605–1612. <https://doi.org/10.1002/jcc.20084>.
44. Sanchez-Garcia, R., Gomez-Blanco, J., Cuervo, A., Carazo, J.M., Sorzano, C.O.S., and Vargas, J. (2021). DeepEMhancer: a deep learning solution for cryo-EM volume post-processing. *Commun. Biol.* *4*, 874. <https://doi.org/10.1038/s42003-021-02399-1>.
45. Liu, J., Taylor, D.W., Kremntsova, E.B., Trybus, K.M., and Taylor, K.A. (2006). Three-dimensional structure of the myosin V inhibited state by cryo-electron tomography. *Nature* *442*, 208–211. <https://doi.org/10.1038/nature04719>.
46. Beckers, M., and Sachse, C. (2020). Permutation testing of Fourier shell correlation for resolution estimation of cryo-EM maps. *J. Struct. Biol.* *212*, 107579. <https://doi.org/10.1016/j.jsb.2020.107579>.
47. Mirdita, M., Schütze, K., Moriawaki, Y., Heo, L., Ovchinnikov, S., and Steinegger, M. (2022). ColabFold: making protein folding accessible to all. *Nat. Methods* *19*, 679–682. <https://doi.org/10.1038/s41592-022-01488-1>.
48. Croll, T.I. (2018). ISOLDE: a physically realistic environment for model building into low-resolution electron-density maps. *Acta Crystallogr. D Struct. Biol.* *74*, 519–530. <https://doi.org/10.1107/S2059798318002425>.
49. Waterhouse, A., Bertoni, M., Bienert, S., Studer, G., Tauriello, G., Gumienny, R., Heer, F.T., de Beer, T.A.P., Rempfer, C., Bordoli, L., et al. (2018). SWISS-MODEL: homology modelling of protein structures and complexes. *Nucleic Acids Res.* *46*, W296–W303. <https://doi.org/10.1093/nar/gky427>.
50. Case, D.A., Aktulga, H.M., Belfon, K., Ben-Shalom, I.Y., Berryman, J.T., Brozell, S.R., Cerutti, D.S., Cheatham, T.E. I., Cisneros, G.A., Cruzeiro, V.W.D., et al. (2020). Amber. <https://ambermd.org/>.
51. Tian, C., Kasavajhala, K., Belfon, K.A.A., Raguette, L., Huang, H., Miguels, A.N., Bickel, J., Wang, Y., Pincay, J., Wu, Q., and Simmerling, C. (2020). ff19SB: Amino-Acid-Specific Protein Backbone Parameters Trained against Quantum Mechanics Energy Surfaces in Solution. *J. Chem. Theor. Comput.* *16*, 528–552. <https://doi.org/10.1021/acs.jctc.9b00591>.
52. Humphrey, W., Dalke, A., and Schulten, K. (1996). VMD: visual molecular dynamics. *J. Mol. Graph.* *14*, 33–38. 27–28. [https://doi.org/10.1016/0263-7855\(96\)00018-5](https://doi.org/10.1016/0263-7855(96)00018-5).
53. Chen, V.B., Arendall, W.B., 3rd, Headd, J.J., Keedy, D.A., Immormino, R.M., Kapral, G.J., Murray, L.W., Richardson, J.S., and Richardson, D.C. (2010). MolProbity: all-atom structure validation for macromolecular crystallography. *Acta Crystallogr. D Biol. Crystallogr.* *66*, 12–21. <https://doi.org/10.1107/S0907444909042073>.
54. Emsley, P., Lohkamp, B., Scott, W.G., and Cowtan, K. (2010). Features and development of Coot. *Acta Crystallogr. D Biol. Crystallogr.* *66*, 486–501. <https://doi.org/10.1107/S0907444910007493>.
55. Hutter, J.L., and Bechhoefer, J. (1993). Calibration of atomic-force microscope tips. *Rev. Sci. Instrum.* *64*, 1868–1873. <https://doi.org/10.1063/1.1143970>.
56. Harris, C.R., Millman, K.J., van der Walt, S.J., Gommers, R., Virtanen, P., Cournapeau, D., Wieser, E., Taylor, J., Berg, S., Smith, N.J., et al. (2020). Array programming with NumPy. *Nature* *585*, 357–362. <https://doi.org/10.1038/s41586-020-2649-2>.
57. Van Rossum, G., and Drake, F.L. (2009). *Python 3 Reference Manual (CreateSpace)*.
58. Virtanen, P., Gommers, R., Oliphant, T.E., Haberland, M., Reddy, T., Cournapeau, D., Burovski, E., Peterson, P., Weckesser, W., Bright, J., et al. (2020). SciPy 1.0: fundamental algorithms for scientific computing in Python. *Nat. Methods* *17*, 261–272. <https://doi.org/10.1038/s41592-019-0686-2>.
59. Hunter, J.D. (2007). Matplotlib: A 2D Graphics Environment. *Comput. Sci. Eng.* *9*, 90–95. <https://doi.org/10.1109/MCSE.2007.55>.

STAR★METHODS

KEY RESOURCES TABLE

REAGENT or RESOURCE	SOURCE	IDENTIFIER
Chemicals, peptides, and recombinant proteins		
Myosin-5a + FLAG tag	Gifted by Howard White.	N/A
Calm1 (CaM)	Gifted by Howard White.	N/A
Rabbit Skeletal Muscle G-Actin	This paper, or Cytoskeleton Inc	Cat# SKU:AKL99
Adenosine 5'-Triphosphate, Disodium Salt	Merck	Cat# 34369-07-8
Quantifoil R2/2 Cu 300 mesh grids	Agar Scientific	Cat# AGS173-2
Whatman® Quantitative filter paper, ashless, Grade 42	Cytiva	Cat# 1442-055
Deposited data		
Class a	This paper	EMDB: EMD-16846
Class b	This paper	EMDB: EMD-16848
Class c	This paper	EMDB: EMD-16849
Class d	This paper	EMDB; EMD-16850
Class e	This paper	EMDB: EMD-16851
Class f	This paper	EMDB: EMD-16853
Class g	This paper	EMDB: EMD-16852
Class h	This paper	EMDB: EMD-16854
Class i	This paper	EMDB: EMD-16855
Pseudoatomic model (class d)	This paper	PDB: 8OF8
Reconstruction focusing on the motor domain plus 2IQs	This paper	EMDB: EMD-16856
Software and algorithms		
MotionCor2	Zheng et al. 2017 ⁴⁰	https://emcore.ucsf.edu/ucsf-motioncor2
Gctf	Zhang et al. 2017 ⁴¹	N/A
Relion 3.1	Zivanov et al. 2018 ⁴²	https://www3.mrc-lmb.cam.ac.uk/relion/index.php/Main_Page
Chimera	Petterson et al. 2004 ⁴³	https://www.cgl.ucsf.edu/chimera/
DeepEMhancer	Sanchez-Garcia et al. 2021 ⁴⁴	https://github.com/rsanchezgarc/deepEMhancer
Statistical post-processing of cryo-EM maps (SPOC)	Beckers & Sachse 2020 ⁴⁶	https://er-c.org/index.php/software/cryo-em/spoc/
AlphaFold 2.0	Mirdita et al. 2020 ⁴⁷	https://colab.research.google.com/github/deepmind/alphafold/blob/main/notebooks/AlphaFold.ipynb
Isolde	Croll 2018 ⁴⁸	https://tristanic.github.io/isolde/
SWISS-MODEL	Waterhouse et al. 2018 ⁴⁹	https://swissmodel.expasy.org/
Amber20	Case 2020 ⁵⁰	https://ambermd.org/
Visual molecular dynamics (VMD)	Humphrey et al. 1996 ⁵²	https://www.ks.uiuc.edu/Research/vmd/
MolProbity	Chen et al. 2010 ⁵³	http://molprobity.biochem.duke.edu/index.php
Python 3	Van Rossum & Drake 2009 ⁵⁶	https://www.python.org/
NumPy	Harris et al. 2020 ⁵⁷	https://numpy.org/
SciPy	Virtanen et al. 2020 ⁵⁸	https://scipy.org/
Matplotlib	Hunter 2007 ⁵⁹	https://matplotlib.org/
Other		
GloQube	Quorum Technologies	N/A
Vitrobot Mark IV	Thermo Fisher	N/A
FEI Titan Krios	FEI	N/A
Falcon III detector	FEI	N/A

EXPERIMENTAL MODEL AND STUDY PARTICIPANT DETAILS

Insect Sf9 cells (RRID: CVCL_0549) were used for expression of murine Myo5a and CaM. Expression and purification were performed by the laboratory of Prof. Howard White (East Virginia Medical School, USA) and the purified proteins were gifted to us for the experiments reported here. Rabbit skeletal muscle was used for globular actin (G-actin) purification.

METHOD DETAILS

Sample preparation

The murine Myo5a S1 construct (residues 1-907 followed by a FLAG-tag, cloned into a pFastbac plasmid (Thermo Fisher Scientific) and CaM proteins were purified as described^{37,38} and stored in liquid nitrogen (LN₂). Both proteins were kindly provided to us by Howard White (East Virginia Medical School, USA). Briefly, Myo5a and CaM were co-expressed using a baculovirus/Sf9 cell system following the protocol provided by the manufacturer (Thermo Fisher Scientific) and purified using FLAG-affinity chromatography. Rabbit skeletal muscle G-actin stocks were purified from acetone powder of rabbit back and leg muscle as described.³⁹ Alternatively, G-actin (>99% pure) purified in the same way can be purchased from Cytoskeleton Inc. G-actin was dialyzed into 0.2 mM CaCl₂, 0.5 mM DTT, 0.2 mM ATP, and 2 mM Tris-HCl, at pH 8.0, and stored in LN₂.

After thawing stored CaM bound Myo5a S1, excess CaM was added in a 2:1 molar ratio of CaM to Myo5a to ensure all IQ motifs were fully occupied. After thawing, G-actin was polymerized on ice, by first exchanging Ca²⁺ for Mg²⁺ in exchange buffer (final solution concentrations: 1 mM EGTA, 0.27 mM MgCl₂) followed by polymerization in polymerization buffer (final solution concentrations: 25 mM KCl, 1 mM MgCl₂, 1 mM EGTA, 10 mM MOPS, pH 7.0) overnight on ice.

Grid preparation and cryo-EM data acquisition

Quantifoil R2/2 carbon Cu 300 mesh grids (Agar Scientific, Stansted, UK) were glow discharged in an amylamine vapour at 20 mA for 30 s (GloQube, Quorum Technologies Ltd, Laughton, UK). Directly before application, F-actin was sheared by being repeatedly drawn up and ejected with a gel-loading pipette tip to shorten filaments, to increase the amount of F-actin observed occupying grid holes. 1 μ L of sheared F-actin (0.5 μ M) was applied to the grid and incubated for 2 mins. 3 μ L of Myo5a S1 supplemented with CaM (3.3 μ M + 6.7 μ M, respectively) was added to the grid in the Vitrobot Mark IV (ThermoFisher, Altrincham, UK), followed by a second incubation of 2 mins. Final concentrations of proteins were: 0.125 μ M actin, 2.5 μ M Myo5a S1 5 μ M CaM. All dilutions were done using 100 mM KCl, 0.1 mM EGTA, 1 mM MgCl₂, 10 mM MOPS, pH 7.0. Grids were then blotted for 3 s at blot force -25 with Whatman no. 42 Ashless filter paper (Agar Scientific, Stansted, UK), to reduce the risk of Ca²⁺ causing CaMs to dissociate, at 8 °C and 80 % humidity. Following blotting grids were drained for 0.5 s and flash-frozen in liquid ethane. Grid preparation procedures were optimised around previously published methods for Myo5a.^{16,32} Data was recorded on the FEI Titan Krios I (Astbury Biostructure Laboratory, University of Leeds, Leeds, UK) equipped with a FEI Falcon III detector operating in linear mode (Table S2).

Cryo-EM image processing

First, MotionCor2⁴⁰ was used to correct for beam-induced motion, and the contrast transfer function (CTF) was estimated using Gctf (GPU accelerated CTF),⁴¹ before subsequent processing steps (Figure S9). The start-end coordinates of F-actin filaments were manually picked using RELION 3.1 (Figure S9B).⁴² Particles were extracted in RELION 3.1 using helical parameters (box size 608 px, helical rise 27.5 Å, tube diameter 250 Å). The data was initially binned to 2.13 Å. Helical 3D refinement was used to produce an initial model (tube outer diameter 140 Å, angular search range tilt 15° and psi 10°, initial twist -166.15°, helical rise 27.5 Å, twist search -165° to -167° with a 0.1° step, rise search 26.5 Å to 28.5 Å with a 0.1 Å step) (Figure S9C). A known structure of the Myo5a motor (PDB: 7PLU¹⁶) was rigid fit into the helical refinement map at a motor domain that was the best resolved and positioned at the centre of the box, using Chimera.⁴³ A map of the fitted PDB structure was generated in Chimera⁴³ and used as an input to generate a wide mask of the motor domain in RELION 3.1 for masked 3D classification.⁴² Masked 3D classification was performed in RELION 3.1 to classify out undecorated F-actin and to only include particles with myosin bound at the centre of the box (5 classes, no image alignment, regularization parameter T = 4) (Figure S9D). This dataset was then un-binned (1.065 Å) as initial reconstructions were reaching the Nyquist limit. 3D helical refinement followed by masked post-processing of this subset of particles produced a map with a 3.8 Å global resolution, but with limited detail across the lever (Figure S9C). All global resolutions were determined using the gold standard Fourier Shell Correlation (FSC) reported to FSC = 0.143 (FSC_{0.143}) using RELION 3.1. To compare the motor domain to the previously published chicken actomyosin-5a rigor structure (PDB: 7PLU¹⁶), particle subtraction was performed subtracting all density outside of a mask comprising of the motor, the first 2 CaMs and 3 F-actin subunits. 3D refinement followed by post-processing, produced a map with a global resolution of 4.2 Å according to the FSC_{0.143}-criterion (Figure S9E), which was similar to that previously published (3.2 Å, PDB: 7PLU¹⁶) (Figure S3). This map was then locally sharpened using DeepEMhancer.⁴⁴

To improve lever resolution, particle subtraction was required to aid particle alignment and centralize the lever domain within the box. It was noted from initial 3D helical reconstructions that the lever density was smeared, so a wide mask containing 1 actin subunit, the motor, and a cone shape for the lever to accommodate flexibility was used for subtraction (Figure S9F). A map was generated in Chimera comprising a single actin subunit, a motor (both from PDB: 7PLU¹⁶), and multiple copies of a Myo5a lever model (PDB: 2DFS⁴⁵) arranged in a cone shape tapering at the motor and splaying towards the lever end. These were positioned so that the boundaries of the cone met the density of the neighboring F-actin bound heads in the helical map. A wide cone-shaped mask

was generated in RELION 3.1 using the cone-shaped map (Figure S9F). The signal outside of this mask was subtracted from the binned (to 2.13 Å) 2D images, and particles were re-centered bringing the lever to the focal point of the box. 3D refinement of the subtracted particles produced a map (cone subtracted map) with 4.3 Å global resolution according to the FSC_{0.143}-criterion (Figure S9G). This map was locally sharpened using DeepEMhancer.⁴⁴ The cone subtracted map had improved resolution across the lever, however defined density for CaMs 5 and 6 could not be seen (Figure S9G).

To resolve CaMs 5 and 6, 3D classification of the lever domain using a cone shaped lever mask was performed. This mask was generated in the same way, but the actin subunit and motor domain were excluded to classify based on lever conformation only. Attempts to classify into 10 or 20 classes both resulted in ~9 reasonable classes (Figure S9H). These conformations reconstructed by 3D classification are not distinct conformational states but representative of continuous thermally driven motion of the lever, as the conformation of the classes produced differed in both modes of division (10 or 20). Much larger numbers of particles may have resulted in a larger number of classes. The maps were locally sharpened using DeepEMhancer.⁴⁴ Though classification led to a reduction in overall resolution due to loss of particles in the reconstruction, we were able to see across the full length of the lever while the motor is actin bound (Figure S9I). However, we cannot rule out that there may be particles representing more extreme lever conformations outside of the subtraction and classification masks used to focus the image processing.

The cryo-EM 3D class with the best global resolution (7.5 Å) (Figures S9I and S1A) was selected to build a pseudoatomic lever model (Figure 1D). The local resolution of this map was calculated using SPOC (statistical post-processing of cryo-EM maps) (Figure S1B), as the local resolution calculations in RELION are unreliable at resolutions lower than 10 Å.⁴⁶

All maps displayed in the figures have been locally sharpened using DeepEMhancer.⁴⁴

Cryo-EM model building and refinement

An initial lever model including the converter + 6IQ motifs sequence (698-907) + 8 residue FLAG-tag, and 6 CaM sequences, was built in AlphaFold 2.0 using CollabFold Google collab notebooks.⁴⁷ This model was then flexibly fit into the density of the best 3D class (σ) using Isolde,⁴⁸ applying distance and torsional restraints taken from murine IQ1-2 and CaM structure (PDB: 2IX7³¹) to each CaM pair. Distance and torsional restraints from the Myo2p 25-residue spaced pair structure (PDB: 1N2D¹⁸) were applied to interacting residues in 25 residue spaced pairs (Glu14-Arg91, in CaM2-3 and CaM4-5), as density corresponding to these interactions could be seen in the selected class (σ) map. Only the C-lobe of CaM6 was included in fitting as only density for this half of the molecule could be seen in the map. To model the N-lobe of CaM6 a homology model of CaM in an extended state, based on a Myo2p-Mlc1p structure (PDB: 1M46¹⁹), was built using SWISS-MODEL.⁴⁹ The sequence identity between human CaM and yeast Mlc1p is 33.57% (Figure S10). The C-lobe of the homology model was superimposed onto the C-lobe of the initial CaM6 model. The N-lobe (residues 3-84) of the homology model was then joined to the C-lobe of the initial CaM6 model and minimized in Isolde without map weighting.

A pseudoatomic lever model was generated by performing all-atom MD simulations of the fitted lever model to gain side-chain conformations. All simulations were performed using Amber20⁵⁰ with the FF19SB forcefield.⁵¹ The lever model was protonated according to the Amber residue templates and then solvated with TIP3P water molecules in an octahedral box that extended 14 Å from the protein. An octahedral box was chosen as it is the closest shape to a sphere, recommended for elongated molecules such as the Myo5a lever. K⁺ ions were added to neutralize the system, then KCl was added to a final concentration of 100 mM. After initial energy minimization the system was heated to 300 K as positional restraints were decreased from 100 to 0 kcal/mol/Å², except for across the lever heavy chain. A restraint of 1 kcal/mol/Å² was applied to the backbone of the lever heavy chain throughout the minimization, equilibration, and production runs, to permit CaM motion and interaction with the heavy chain side-chains but maintain the lever position seen in the cryo-EM map. Minimization and equilibration steps were performed on the ARC4 standard nodes (Intel Xeon Gold 6138 CPUs ('Sky Lake')). NMR distance restraints were also applied between interactions visible in the cryo-EM density (Glu14Arg90). To do this, distance restraints were applied between the C δ atom of Glu, and C ζ of Arg, to not dictate which N and O interact. These were weighted at 20 kcal/mol/Å² within 1.9 Å of the bounds of the flat well restraint (3.4-5.3 Å), and a 20 kcal/mol/Å² harmonic potential was applied outside of this range. The MD production runs used the pmemd.cuda module from Amber20 and were run on Bede using Tesla V100 GPUs. MD was performed for 300 ns in triplicate repeat. The Berendsen Thermostat was used as recommended to maximize GPU performance. To compare the flexibility of each CaM, per residue root mean square fluctuation (RMSF) analysis was performed using CPPTRAJ on each CaM for all three repeat simulations.³⁶

Following simulation, the average conformation was calculated in VMD (Visual Molecular Dynamics),⁵² and the frame of the trajectory with the lowest global RMSD (Root Mean Square Deviation) with the average conformation was selected as a model for each repeat. A further round of minimization was then performed on the ARC4 general nodes to restore sidechains to low energy conformations. After minimization, each model was scored in MolProbity,⁵³ and the repeat with the lowest MolProbity score and the largest proportion within the cryo-EM density was selected as the final lever model.

To generate a model of the motor domain, a homology model of murine Myo5a was made using the chicken actomyosin-5a rigor structure (PDB:7PLU¹⁶) as the template in SWISS-MODEL.⁴⁹ The sequence identity between mouse and chicken Myo5a is 94.61% (Figure S11). This was then fit into the cryo-EM density using Isolde,⁴⁸ applying distance and torsional restraints based on the template. Residues 1-698 were then joined to the pseudoatomic lever model (699-915). The regularize zone tool in Coot was used to correct over the stitch region.⁵⁴ The F-actin subunits from the chicken actomyosin-5a rigor structure (PDB:7PLU¹⁶), with phalloidin removed, were also fit into the density corresponding to actin using Isolde.⁴⁸ As the resolution of F-actin and the motor domain was insufficient to fit side-chains, and their structures have already been published at high-resolution, only the backbone is included for these domains in our model. Side-chain orientations are included for the lever from the simulated data. The quality of the final model

was assessed using MolProbity⁵³ (Table S3). The fit of the model within the map was scored using the PDB atom inclusion scores (Table S4).

Flexibility analysis

All flexibility analyses were performed on discretized representations of Myo5a S1. First the Isolde generated lever model (pre-simulation) and the homology model of the motor were flexibly fit into each cryo-EM class with torsional and distance restraints applied using Isolde.⁴⁸ The fits of the models within the class maps were scored using the PDB atom inclusion scores (Table S4). A coarse-grained representation of the conformation of Myo5a S1 was then defined by discretizing into 8 vectors (Figure 4A) drawn between C α atoms for the base (actin binding interface) (res 384 and 543), the converter (res 721 and 760), and CaMs 1-6 (res 137 and 64) (Figure S6A).

There are several different ways in which the bending stiffness of the lever arm can be quantified. Treating the entire lever as acting as a single spring, we can define an overall bending stiffness, k_{ov} that corresponds to the perpendicular force at the end of the lever divided by the displacement at the end of the lever. This allows comparison with previous measurements of lever stiffness and is therefore measured in units of pN nm⁻¹. To look in more detail at where this flexibility arises, it is useful to also examine the local resistance to bending: the flexural rigidity, EI , which can vary along the length of the lever. This is the ratio of the bending torque at that particular location to the local rate of change of the orientation angle with respect to distance, s , along the lever and so has units of pN nm².

The general equation relating the local angle of deflection of the beam, $\theta(s)$ to the moment, $M(s)$ at this point is given by,

$$EI \frac{\partial \theta}{\partial s} = M(s). \quad (\text{Equation 1})$$

If the lever is a cantilever clamped at $s=0$ and deflected by a perpendicular force $F \sin \theta_{act}$ at the end $s=L$, the moment is given by Equation 2,

$$M(s) = F \sin \theta_{act} (L - s). \quad (\text{Equation 2})$$

Thus, for a beam of uniform flexural rigidity, the bending stiffness is $k_{ov}=3EI/L^3$.

The overall bending stiffness of the entire lever was calculated using the variance in lever displacement from the mean. First, a vector representing the lever was drawn between the midpoint of the converter, and the midpoint of CaM6 for all classes (Figure S5A). The mean of these lever vectors was then used to define a new coordinate system with an origin at the midpoint of the converter (Figure 3C) and the z-axis along the mean direction of the lever (Figure S5A). The x and y axes in the perpendicular plane were defined such that changes in y represented tilt motions (towards the F-actin longitudinal axis) and changes in x presented slew motions (perpendicular to the F-actin axis). Thus, the y-axis was orthogonal to z, and the yz plane was parallel to the vector representing F-actin (res 179 C α atom of the 0th and 13th subunit of a model F-actin). The model of F-actin was made by fitting an actin subunit from a previously published structure into the 0th and 13th subunit of our initial F-actin helical reconstruction (Figure S9C). Then for each class, the distance, d_c , in the xy plane between the end point of the lever vector and the end point of the mean vector was calculated for each class (Figure S5). The variance in lever conformation was calculated using Equation 3,

$$\sigma_{3D}^2 = \frac{\sum_{c=1}^a n_c d_c^2}{\sum_{c=1}^a n_c}, \quad (\text{Equation 3})$$

where n_c is the number of particles in the class. This was done for the overall displacement, and for displacement in a particular direction (tilt and slew, along the y- and x-axes respectively), to calculate the overall bending stiffness (Figure S5B) and the bending stiffness in both directions (tilt/slew, Figure S5C).

From the principle of equipartition of energy,⁵⁵ the overall cantilever bending stiffness (k_{ov}) can be calculated when no force is applied using the observed variance in lever position caused by thermal fluctuation. This was calculated using Equation 3,

$$k_{ov} = \frac{2k_B T}{\sigma_{3D}^2}, \quad (\text{Equation 4})$$

where $k_B = 1.38 \times 10^{-23}$ N m K⁻¹ (Boltzmann constant), $T = 281$ K (temperature used to make EM grids for actomyosin in Kelvin), L is the mean length of the lever vectors (20.4 nm), and σ_{3D}^2 is the variance calculated from the overall displacement within the 2 degrees of freedom. A factor of 2 is included in Equation 3 to account for the two degrees of freedom in bending along two perpendicular directions.

We also calculated a separate directional cantilever bending stiffness ($k_{dir,i}$) for displacements in the x and y directions separately using Equation 5,

$$k_{dir,i} = \frac{k_B T}{\sigma_i^2}, \quad (\text{Equation 5})$$

where σ_i^2 are the variances calculated from the displacements in x or y.

The Pearson's correlation coefficient for a sample population was determined using Equation 5,

$$\text{correlation} = \frac{\sum_{c=1}^a n_c x_c y_c}{\sqrt{\sum_{c=1}^a x_c^2 y_c^2}}, \quad (\text{Equation 6})$$

where (x_c, y_c) is the displacement between the class and mean vector in the xy plane.

To estimate the error in the calculation of the cantilever bending stiffness we simulated the effect of uncertainties in lever position caused by grouping of molecules into classes. Here we assume that the uncertainty of lever position within a class is of the same order of magnitude as the difference in displacement between classes. Our procedure is as follows: the values for displacement from the mean of each class were sorted into ascending order. For each class, the difference in displacement between classes either side of it were calculated, to give the potential errors in lever position. For classes with a single neighbour at the start or end of the list, the bounds were \pm the difference in displacement from their single neighbour. Then, for each class, a new lever position was calculated by choosing a random position within these bounds. The new randomly generated positions were used to calculate the unweighted variance using Equation 7,

$$\text{lever variance} = \frac{\sum_{c=1}^a d_c^2}{9}, \quad (\text{Equation 7})$$

where d_c is the randomly generated displacement. Unlike for the cryo-EM conformations, the variance could not be weighted by particle class occupancy. This variance was then used to calculate the bending stiffness using Equation 4 for the overall bending stiffness and Equation 5 for the directional bending stiffness in each direction. This process of generating random positions was repeated 1000 times, generating a new estimate of the bending stiffness each time. The standard deviation of these randomly obtained bending stiffnesses was quoted as the error.

To determine the local conformation of lever subdomains in each class, the 8 vectors representing Myo5a S1 were paired into 7 subdomains. Local material axes uvw were defined for each subdomain (Figures S6A–S6E), where the u axis is the vector between the position vector of the midpoints of neighbouring subdomains and the v and w axes are in the orthogonal plane to u are defined such that the first vector of the subdomain pair lies halfway between v and w (i.e. at an angle of 45°). The angles between the subdomain vector pairs were then calculated in each plane (vw , vu and wu), $\theta_{vw} = \theta$, $\theta_{vu} = \theta_1 - \theta_2$, $\theta_{wu} = \theta_3 - \theta_4$ (Figures S6C–S6E and S7A–S7C), the angles for θ and θ_{1-4} were taken from -90 to 90° . To determine if the distance between CaM interacting regions has an influence on the flexural rigidity, the distance between the $C\alpha$ atoms of known interacting residues in the N- and C-lobe of consecutive CaMs was calculated (Ser17 and Asn111, respectively) (Figure S7D).

To calculate the flexural rigidity of the subdomains (E), we looked at the change of angle between the subdomain pairs with respect to the distance between them. The variance (σ^2) in angle between subdomain vector pairs within the classes (weighted by the number of particles in each class) was calculated in 3 orthogonal planes (vw , vu , wu) (Figures S6A–S7E and S7A–S7C). The variation in the vw plane describes twist (torsion) (Figures S6C and S7C), and the vu and wu planes describe bending stiffness in 2 directions (Figures S6D, S6E, S7A, and S7B). E_i in each plane was calculated using Equation 8,

$$E_i = \frac{L_{sub} k_B T}{\sigma^2}, \quad (\text{Equation 8})$$

where L_{sub} is the average length of the subdomain in the cryo-EM 3D classes (the distance between the position vector of the midpoints of neighbouring subdomains, Table S5) and σ^2 is the variance in angle between subdomain vector pairs within the classes. The flexural rigidity was calculated by averaging the values in the vu and wu plane.

To estimate the error in the calculation of the flexural rigidity we simulated the effect of uncertainties in lever subdomain conformation caused by grouping of molecules into classes. Here we assume that the uncertainty of lever subdomain conformation within a class is of the same order of magnitude as the difference in subdomain conformation between classes. For each subdomain, the angles calculated between the vector pair in each class were sorted into ascending order. For each class, the difference in angle between classes either side of it were calculated to give the potential errors in subdomain conformation. For classes with a single neighbour at the start or end of the list, the bounds were \pm the difference in subdomain angle from their single neighbour. The new randomly generated conformations were used to calculate the unweighted variance (σ^2), which was used to calculate a flexural rigidity using Equation 7. This process of generating random conformations was repeated 1000 times for each subdomain, generating a new estimate of the flexural rigidity each time. The standard deviation of these randomly obtained flexural rigidities was quoted as the error.

The deflection of the lever end, D , from its average position when a force is applied to the end is given by,

$$D = \frac{F \sin \theta_{act}}{k_{ov}}. \quad (\text{Equation 9})$$

Here the perpendicular force is $F \sin \theta_{act}$, where F is the force applied, and θ_{act} is the angle between the mean lever position and F-actin (Figure S12A). As in optical trap studies, the force is parallel to the F-actin axis, and it was necessary to determine the deflection when an off-axis (not in the xy plane Figure 3C) force was imposed using $F \sin \theta_{rig}$.

The equivalent distance of the lever deflection along the F-actin axis was also determined using Equation 10,

$$\text{deflection along actin} = D \sin \theta_{act}, \quad (\text{Equation 10})$$

where D is the deflection in the xy plane Figure 3C.

For a cantilever of uniform flexural rigidity, EI , the deflection of the beam from its equilibrium position at a distance s from the fixed end (the converter in our model) can be found from the solutions of Equations 1 and 2 and is given by Equation 11,

$$d(s) = \frac{F \sin \theta_{act} s^2}{6EI} (3L - s). \quad (\text{Equation 11})$$

Predicting the working stroke

The ensemble of lever conformations in the cryo-EM 3D classes were used to predict the working stroke of Myo5a S1. To determine the distance the working stroke translates the end of the lever along F-actin longitudinal axis, a vector between the 0th and 13th subunit (C α , residue 179) of F-actin was calculated from an F-actin model (as above) (Figure S8). The lever models generated from each cryo-EM class were superimposed onto the converter (699-750) of a pre-powerstroke (PDB: 4ZG4³²), and post-powerstroke ADP bound structure (PDB: 7PM6¹⁶) (Figure S8). As 4ZG4 is not actin bound, to model the motor bound in the ADP-P_i (pre-powerstroke) state the L50 domain (residues 490-530) of 4ZG4 was superimposed with the actin interacting region of the L50 domain (residues 492-532) of 7PM6 (Figure S8), as the L50 domain interaction with F-actin is conserved between the ADP-P_i and ADP state.³³ As we do not have density for the CaM6 N-lobe in our Myo5a S1 map, but we believe it interacts with the heavy chain in the full-length motor, we use the equivalent residue in IQ6 (res 912) to the last residue in IQ2 that CaM interacts with in the CaM bound IQ1-2 crystal structure (PDB: 2IX7³¹) as our lever end (Figure S8). Vectors were drawn between the lever end of each class model of the ADP-P_i state to every other class model of the ADP state (Figures 5A and S8). The translation of the lever end along F-actin was calculated using Equation 12,

$$\text{distance along actin} = L_{str} \cos \theta_{str}, \quad (\text{Equation 12})$$

where L_{str} is the magnitude of an ADP-P_i to ADP lever end vector and θ_{str} is the angle between this vector and the F-actin axis (Figure S12B). This was then repeated to calculate the working stroke from the ADP-P_i state models and our rigor models. The probability of a combination of classes being paired was calculated by taking the probability of an individual class occurring, using the fraction of particles in each class out of the total number of particles. The probabilities of each class in a pair were then multiplied to give the probability of that combination of classes being paired.

QUANTIFICATION AND STATISTICAL ANALYSIS

Cryo-EM data collection and processing were performed as described in the cryo-EM image processing section of method details using RELION 3.1,⁴² MotionCor2,⁴⁰ Gctf,⁴¹ and SPOC⁴⁶ as detailed in the key resources table. The root mean square fluctuation of each CaM across the pseudo-atomic model simulation was calculated using CPPTRAJ,³⁶ and is displayed in Figure 2. Statistical analysis of the pseudo-atomic model was performed using MolProbity⁵³ as described in the cryo-EM model building and refinement section of Method Details. The fit of the models within the maps was scored using the PDB atom inclusion scores. Data collection and refinement statistics are summarised in Tables S3 and S4 and Figure S9.

Pearson's Correlation was used to determine the correlation between tilt and skew motions, details can be found in the Flexibility analysis section of Method Details. The standard deviation of the random error was reported as the error for the overall bending stiffness and flexural rigidity calculations, these values are reported in Figure 4, Table S1 and Figure S6, details can be found in the Flexibility Analysis section of Method Details. The mean and the standard deviation of the subdomain conformations were calculated using the NumPy⁵⁶ Python 3⁵⁷ library, and are reported in Figure S7.

Gaussian distributions were fit to the working stroke prediction data using the SciPy⁵⁸ Python 3⁵⁷ library, displayed in Figure 5. All graphs were plotted using Matplotlib.⁵⁹